CFD modelling to derive U-values for floating PV technologies with large water footprint

Dag Lindholm [*], Josefine Selj, Torunn Kjeldstad, Hallvard Fjær, Vilde Nysted

Institute for Energy Technology, Instituttveien 18, 2007 Kjeller, Norway

A B S T R A C T

Floating photovoltaics (FPV) systems are an emerging and increasingly competitive application of solar PV. Although lack of land is the main reason for assessing the technology against land-based PV, favourable cooling conditions, justified by the fact that air above a water body is typically colder and windier than on land, is often also used as an argument. Few have quantified this effect, and the aim of this work has been to use Computational Fluid Dynamics (CFD) to derive U-values for the most used FPV technology today. Our results show that the presence of a float with large water footprint promotes a significant non-uniform temperature field in the wafer layer. The study confirms that the cell temperature rises by decreased wind and by increased solar irradiation and air temperature. We found that the water temperature does not significantly affect the cell temperature. Radiative heat transfer between the back of the module and water was estimated to reduce the cell temperature typically less than 1 °C. Because the technologies are not identical but still represent systems with large water footprint, U-values from the study were considered to compare well to reported values derived from FPV field data in Singapore and the Netherlands.

1. Introduction

Floating photovoltaics (FPV), deployment of PV modules on water bodies, is a rapidly growing niche market for utilization of solar energy to meet the high global demand for energy (Cazzaniga and Rosa-Clot, 2021). From 1.3 GW by the end of 2018, the cumulative capacity of FPV was doubled to approximately 2.6 GW by the end of August 2020 (Where Sun Meets Water, 2019; Haugwitz, 2020). In September 2021 it surpassed 3.0 GW (IEA PVPS, 2021). As the technology matures, the deployment of FPV is expected to continue its impressive growth. A conservative estimate of the global potential of FPV is 400 GW or more (Where Sun Meets Water, 2019). At the turn of the year to 2022, it was reported that the world's largest single water floating PV project with a capacity of 320 MW was launched in Dezhou, in China's Shandong province (Bellini, 2022). The large potential to improve the cost-effectiveness makes co-located and hybrid FPV- and hydropower plants, particularly interesting (Gonzalez Sanchez et al., 2021; Lee et al, 2020).

While the main argument for FPV is lack of available land, other key arguments are loss of efficiency at high operating cell temperature, energy security and decarbonization targets (Oliveira-Pinto and Stokkermans, 2020). As the operating temperature of PV modules affects their efficiency, it is often claimed that floating solar technologies has better efficiency than ground-based systems. Few have quantified this effect. It is often justified by the argument that air above the water body is typically colder and windier than on land. Traditionally, the PV electrical efficiency (η_c) is computed from the linear equation.

$$\eta_c = \eta_{ref}\left[1 - \beta(T_{cell} - T_{ref})\right] \tag{1}$$

where η_{ref} is the cell efficiency at the reference temperature (T_{ref}), β is a temperature coefficient that depends on the cell material, and T_{cell} is the operational cell temperature. Values for η_{ref}, T_{ref} and β are typically provided by the module manufacturer. A list of values has been compiled by Skoplaki and Palyvos (2009). For crystalline silicon cells, the drop in cell efficiency, which is described by the temperature coefficient, is about 0.4–0.5% per 1 °C increment in the cell temperature (Dubey et al., 2013; Fouad et al., 2017; Mohammed et al., 2019; Appelbaum and Maor, 2020).

Many FPV technologies have been developed, some are well established, others are in a pilot test phase. Because of the diversity of technologies, a general assessment of the cooling effect is challenging. However, similarities between many of the technologies allow these to

be classified. According to the degree of water surface coverage of the floats and the capability of air to cool the back of the modules, the various technologies have been categorized into small, medium, and large water footprints (Liu et al., 2018; Dörenkämper et al., 2021). Today, the FPV market is dominated by systems consisting of modular high-density polyethylene (HDPE) float structures that are linked together. Ciel et Terre and Sungrow are the two major companies that provide this type of FPV technologies for installations in high temperature regions. Other providers like Bosch Solar and Mibet Energy have similar solutions based on PV modules installed with a low tilt angle to HDPE float structures. Because these floats cover a relatively large water surface and the module's proximity to water reduces the air flow beneath it, this solution is classified as a technology with large water footprint (Reindl, 2018; Dörenkämper et al., 2021). Due to the widespread use of this FPV system, our work opted for Ciel et Terre's technology to quantify the cooling effect.

The purpose of this study was to use CFD to quantify the enhanced cooling effect achieved by deploying PV modules on a water body. Based on an existing FPV plant in South Africa, the work presents results obtained from Computation Fluid Dynamics (CFD) which provide the operating cell temperatures of individual modules. The cooling effect is quantified by heat loss coefficients or U-values derived from these calculations. Lack of access to experimental data and the necessity to provide confidence in the model results, was solved by performing comparison to NOCT provided by the module manufacturer and to results computed by a simpler heat balance model. The latter model is described in a separate section. U-values for PV modules mounted to Ciel et Terre floats were then derived from a parameter study based on variation in solar irradiation, air temperature, water temperature, and wind speed. Ultimately, the U-values were compared to experimentally based U-values recently reported for FPV technologies with large water footprint (Liu et al., 2018; Reindl, 2018).

2. The computational domain

An existing FPV plant based on Ciel et Terre floats and glass-polymer modules of type Maxpower CS6U 330P (Canadian Solar, 2022), is shown in Fig. 1. Situated in Marlenique, South Africa, the 59.4 kW capacity floating solar system was chosen as basis for our study. It consists of an arrangement of 10×18 PV modules and includes 5 internal walkways to allow for maintenance. Each module has a tilt angle of $15°$.

Modelling the complete system of floats, walkways and PV modules was too ambitious and computational costly, and the computational domain was constructed to include 18 floats arranged in a single row as displayed in Fig. 2. It shows the full-size computational domain, while

Fig. 3 displays a close-up of the floats with and without a module. The latter to reveal the model of the floats. A PV module with dimensions 992 mm $\times$ 1960 mm was fixed to each float. In general, the gusty nature of wind and often rapid change of wind direction requires a three-dimensional (3D) model that includes modules and floats in more than one row, but to limit the scope of our study, not least the size of the computational domain, only the wind direction that is shown in Fig. 2 was accounted for.

Because of symmetry, only half the float including the module was made part of the model. From the PV module short end edge to the facing edge on the neighboring row of modules, the distance was 125 mm. Every third float was followed by a walkway. In Fig. 2, the individual modules are identified by the indices M1-M18, which are used to address the temperatures of the various modules. Similarly, the walkways are identified by W1-W6. Between the walkways, the distance is 4.6 m. The total length of the computational domain was set to 33.6 m, which included a 3.0 m long inlet and outlet section. The height of the domain was set to 2.3 m. Each PV module was modelled with individual layers for the front glass, the encapsulant (EVA), the wafers and a polymer backsheet. Thickness of each layer is listed in Table 1. The wafer layer includes 6×12 cells, but in the model the cells were merged into one large cell with the same dimensions as the module itself. The floats were modelled as a thin-walled geometry filled by air. A total number of 824 000 hexahedral cells were used to discretize the computational domain.

3. Numerical modeling

3.1. Governing equations

Turbulent flow of air past the PV modules was based on the conservation equations of mass and momentum. For incompressible steady-state flow, these equations read.

$$\frac{\partial u_j}{\partial x_j} = 0 \tag{2}$$

$$\frac{\partial (u_i u_j)}{\partial x_j} = -\frac{1}{\rho_0}\frac{\partial p}{\partial x_i} + \frac{\rho - \rho_0}{\rho_0} g_i + \frac{\partial}{\partial x_j}\left[(\nu + \nu_t)\left(\frac{\partial u_i}{\partial x_j} + \frac{\partial u_j}{\partial x_i} - \frac{2}{3}\frac{\partial u_k}{\partial x_k}\delta_{ij}\right)\right] \tag{3}$$

In Eqs. (2)-(3), u_i is the velocity component in direction x_i, p is the pressure, ρ is the air density, ρ_0 is the reference air density, g_i is the gravitational acceleration, ν is the molecular kinematic viscosity, ν_t is the turbulent kinematic viscosity, and δ_{ij} is the Kronecker delta function which is defined as $\delta_{ij} = 0$ $(i \neq j)$ and $\delta_{ij} = 1$ $(i = j)$.

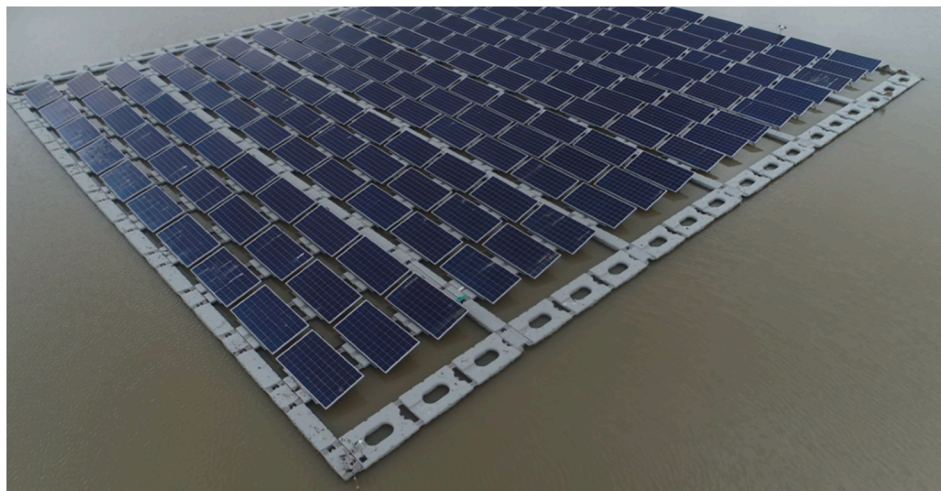Turbulence was modeled using the standard k-ε model, which means

Fig. 1. Ciel et Terre floats deployed on a pond in Marlenique, South Africa.
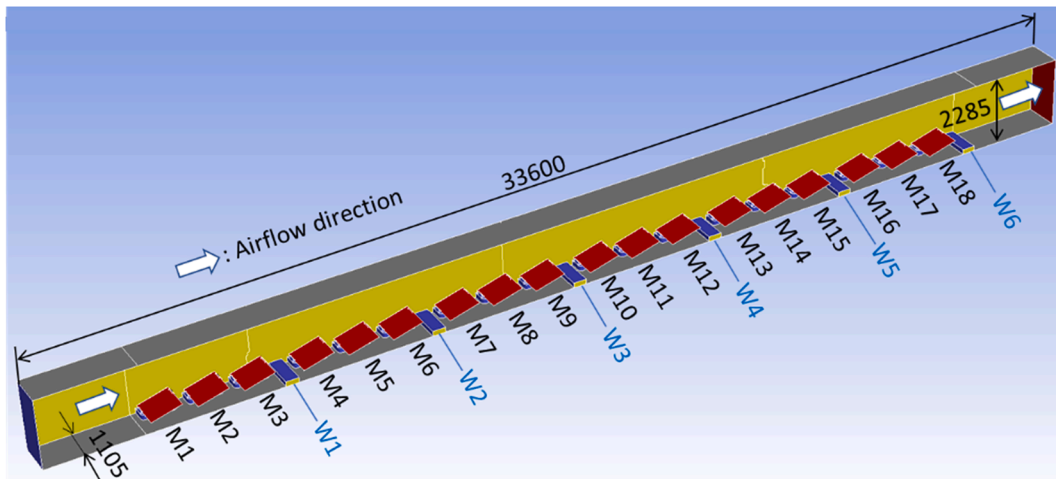
Fig. 2. The computational domain consisting of a row of 18 PV modules in a row. The individual PV modules (M) and walkways (W) are identified by indices.
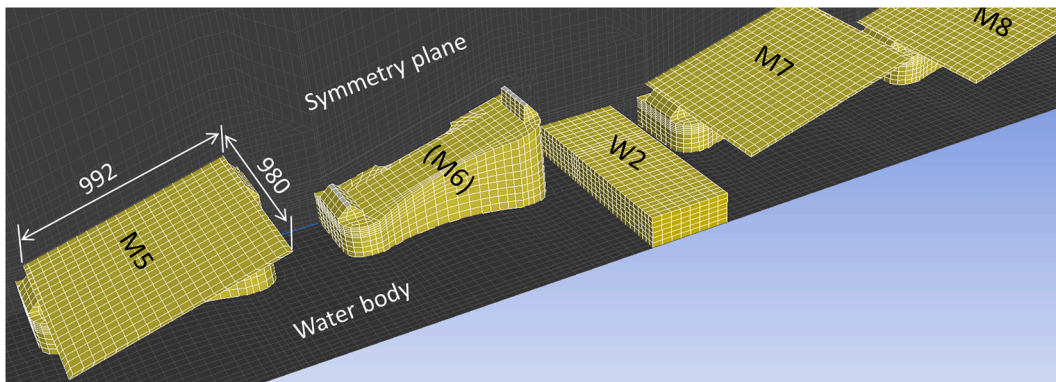

Fig. 3. Model close-up of Ciel et Terre floats with and without a PV module. Mi is the module number in the row, Wi identifies walkways.

Table 1
Thickness and heat conductivity of the various layers in the PV modules.

Module layer	Thickness [mm]	Heat conductivity [W/m·K]
Front cover (glass)	3.2	1.80 (Ogbomo et al., 2018)
Encapsulant (EVA)	0.525	0.21 (Solheim et al., 2013)
Wafer (Silicon)	0.18	148 (Ogbomo et al., 2018)
Backsheet (polymer)	0.175	0.20 (Ogbomo et al., 2018)

that individual transport equations were applied for the turbulent kinetic energy (k) and the turbulent dissipation rate (ε):

$$u_j \frac{\partial k}{\partial x_j} = \frac{\partial}{\partial x_j}\left(\nu + \frac{\nu_t}{C_k}\right)\frac{\partial k}{\partial x_j} + G_k + G_B - \varepsilon \tag{4}$$

$$u_j \frac{\partial \varepsilon}{\partial x_j} = \frac{\partial}{\partial x_j}\left(\nu + \frac{\nu_t}{C_\varepsilon}\right)\frac{\partial \varepsilon}{\partial x_j} + C_{\varepsilon 1}\frac{\varepsilon}{k}[G_k + C_{\varepsilon 3}G_b] - C_{\varepsilon 2}\frac{\varepsilon^2}{k} \tag{5}$$

In Eqs. (4)-(5) the production term G_k, which represents production of turbulent kinetic energy from work done by the interaction of the mean flow and the turbulent stresses, and the buoyancy term G_b, which is based on the Boussinesq approximation, were modelled as.

$$G_k = \nu_t \left(\frac{\partial u_i}{\partial x_j} + \frac{\partial u_j}{\partial x_i}\right)\frac{\partial u_i}{\partial x_j} \tag{6}$$

$$G_b = -g_i \frac{\nu_t}{\rho_0 Pr_t}\frac{\partial \rho}{\partial x_i} \tag{7}$$

In Eq. (7), Pr_t is the turbulent Prandtl number. The turbulent

viscosity, which is not a fluid property, but a variable that depends on the state of the turbulence, was finally computed from.

$$\nu_t = C_\nu \frac{k^2}{\varepsilon} \tag{8}$$

The k-ε turbulence model includes several coefficients with the standard values listed in Table 2 used in this study. The coefficient $C_{\varepsilon 3}$ was computed as.

$$C_{\varepsilon 3} = tanh(u\|/u_\perp) \tag{9}$$

where $u_\perp$ represents the velocity component perpendicular to the gravitational vector and u‖ the velocity component parallel to the gravitational vector.

Temperatures were solved from the conservation of energy equation,

$$\frac{\partial (Tu_j)}{\partial x_j} = \frac{\partial}{\partial x_j}\left[\left(\frac{\nu}{Pr} + \frac{\nu_t}{Pr_t}\right)\frac{\partial T}{\partial x_j}\right] + S_h \tag{10}$$

where T is the temperature, Pr is the Prandtl number, and S_h is the source term that accounts for solar irradiation and energy converted to heat in the wafer layer.

Thermal radiation exchange with the sky and with the water body was accounted for by the Discrete Ordinates (DO) radiation model. This

Table 2
Parameters included in the k-ε turbulence model.

C_k	C_ε	$C_{\varepsilon 1}$	$C_{\varepsilon 2}$	C_ν
1.0	1.3	1.44	1.92	0.09

model solves the radiative transfer equation (RTE) for a finite number of separate solid angles. Each solid angle is associated with a vector direction fixed in the global coordinate system. A review and description of the model is beyond the scope of this work. For simplicity we refer to other works describing the model (Kim and Song, 2010; Filipović et al. 2019; Moreno et al., 2019).

3.2. Boundary conditions

Each of the 6 external sides of the computational domain are identified in Fig. 4. A uniform velocity profile was specified for air that enters through side 1. In the parameter study, the computations account for inlet wind speeds ranging from 1 m/s to 5 m/s and for air temperatures equal to 25 °C and 30 °C. Air leaves through side 2, which was specified as a pressure outlet at atmospheric pressure. The two sides labelled 5 and 6 were both specified by a symmetry condition.

To account for the temperature of the water body and the sky, two subdomains, both 2 cm thick with an artificial large thermal conductivity, were added to the computational domain. These are too narrow to be visible in Fig. 4. The bottom surface of the water body subdomain was given a Dirichlet condition with the temperature set equal to the water temperature. Specification of a heat transfer coefficient at the air–water interface (side 3) was then avoided, instead it was a part of the computation. A similar methodology was applied for side 4, which represents the air-sky interface in the model. The sky temperature, computed from the equation (Swinbank, 1963).

$$T_{sky} = 0.0552\, T_{air}^{1.5} \tag{11}$$

was assigned as a Dirichlet condition for the sky subdomain. The convective heat transfer at the sky-air interface was set to zero, which meant that the air-sky interface (side 4) only contributed to radiative heat transfer in the domain. The emissivity of water, sky and glass was set to 0.96, 0.86 and 0.91 (Hammami et al., 2017; Evangelisti et al., 2019). While a slip condition was specified for the flow field at side 3 (sky), a non-slip condition was set at side 4 (water).

4. Heat balance model

The focus of this work was use of CFD to obtain cell temperatures and U-values for modules mounted to standard Ciel et Terre floats. These floats have a rather complex structure, which influences the air flow and hence heat transfer of the modules. To add confidence in the computations, results are also compared to the heat balance model proposed by Lindholm et al. (2021). Even if the model was derived for FPV, it cannot in the same way as CFD account for the complex structure of the float and how it influences the heat transfer of the modules. However, it can be used to verify the CFD model for a simplified geometry, and to compute U-values for modules exposed to various meteorological

conditions, but without influence of the float. The latter simplification means that module cooling and resulting U-values are overestimated. U-values obtained by CFD are therefore expected to be lower, which is valuable information.

Details about derivation and assumptions made for the heat balance model is beyond the scope of this text, only the main equations are presented here (Lindholm et al., 2021). For a well-ventilated module with air cooling on both external surfaces, the steady-state heat balance can be written as.

$$(\tau\alpha - \eta_c) \bullet G_T = U(T_{cell} - T_{air}) \tag{12}$$

In Eq. (12), U is the heat loss coefficient, G_T is the solar irradiance incident on the module surface, α is the solar absorptance and τ is the transmittance of the module glazing. For simplicity, we neglect heat absorbed by the upper glass and assume that all absorbed heat is absorbed by the wafer. Fig. 5 shows the heat flow paths and heat exchange modes that are included in the model. At the external surfaces, heat is exchanged both by convection and thermal radiation. As indicated in Fig. 5, the thermal model divides the modules into two parts, one upper part and another lower part. The module temperatures – cell (T_{cell}), glass cover (T_{front}) and backsheet (T_{back}) – are computed from the three equations:

$$T_{cell} = \frac{B_{front}B_{back} \bullet (\tau\alpha - \eta) \bullet G_{POA} + A_{front}B_{back}C_{front} + A_{back}B_{front}C_{back}}{B_{front}B_{back}\left(A_{back} + A_{front}\right) - A_{back}^2 B_{front} - A_{front}^2 B_{back}} \tag{13}$$

$$T_{front} = \frac{A_{front}T_{cell} + C_{front}}{B_{front}} \tag{14}$$

$$T_{back} = \frac{A_{back}T_{cell} + C_{back}}{B_{back}} \tag{15}$$

These equations include the three coefficients A_i, B_i and C_i. A_i depends on the build of materials (BOM). This coefficient accounts for heat conduction in the module, while C_i account for convection and radiation at the module external surfaces. The coefficient B_i depends on all three heat transfer mechanisms. The way these coefficients are defined is given in Table 3. Index *front* refers to the module upper half, while *back* refers to the lower half. Applied heat transfer coefficients and the model applied to compute the sky temperature are presented in Table 4.

The thermal model computes the module U-value from the component representing the heat loss through the module upper half and through the lower half. The equation reads.

$$U(T_{cell} - T_{air}) = (U_{back} + U_{front})(T_{cell} - T_{air}) \tag{16}$$

where the overall U-value is computed as the sum of the two components, U_{front} and U_{back}, as.
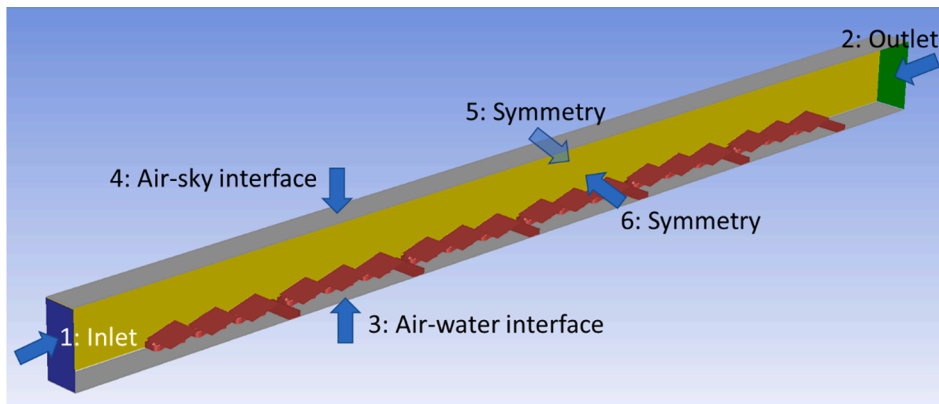

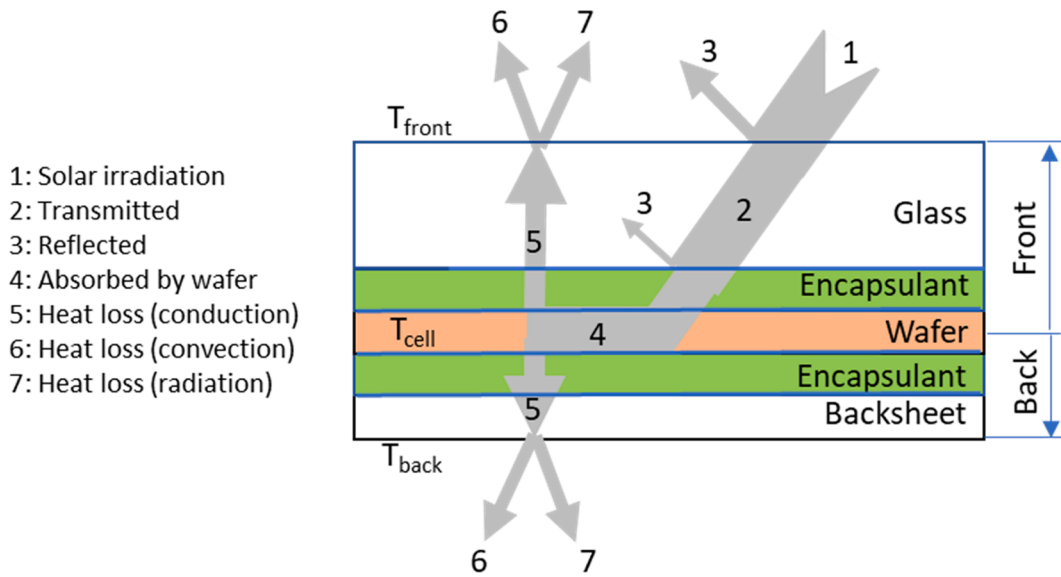**Fig. 4.** Identification of the external sides of the computational domain.

Fig. 5. Heat flow paths and heat exchange modes in the thermal model (Lindholm et al., 2021).

Table 3
Coefficients applied in the heat balance model.

Module upper half:	Module lower half:
$\frac{1}{A_{front}} = \left(\frac{\Delta s_c}{2\lambda_c}\right) + \sum_i \left(\frac{\Delta s_{i,front}}{\lambda_{i,front}}\right)$ (19)	$\frac{1}{A_{back}} = \left(\frac{\Delta s_c}{2\lambda_c}\right) + \sum_i \left(\frac{\Delta s_{i,back}}{\lambda_{i,back}}\right)$ (20)
$B_{front} = A_{front} + h_{air} + h_{sky}$	$B_{back} = A_{back} + h_{air} + h_{wat}$
$C_{front} = h_{air}T_{air} + h_{sky}T_{sky}$	$C_{back} = h_{air}T_{air} + h_{wat}T_{wat}$
Δs_i = Thickness of module layer i (cell, encapsulant, glass, backsheet)	
λ_i = Thermal conductivity of module layer i	
h_i = Heat transfer coefficient (convection to air, thermal radiation to sky and water)	
T_i = Temperature (air, water or sky)	

Table 4
Heat transfer coefficients applied in the heat balance model.

Heat transfer coefficients (air, sky and water):	
$h_{air} = 2.8 + 3 \cdot v_{air}$ (Watmuff, 1977)	(21)
$h_{sky} = \varepsilon_{front}\sigma\left(T_{front}+T_{sky}\right)\left(T_{front}^2+T_{sky}^2\right)$	(22)
$h_{wat} = \varepsilon_{back}\sigma\left(T_{back}+T_{wat}\right)\left(T_{back}^2+T_{wat}^2\right)$	(23)
h_i = Heat transfer coefficient (convection to air or water, thermal radiation to sky)	
T_i = Temperature (module front, air or sky). T_{sky} is computed from Eq. (11)	
v_i = Wind speed	
ε_i = Emissivity (front glass or backsheet)	
$\sigma = 5.67 \cdot 10^{-8}$ W/m^{2}K^4 (Stefan-Boltzmann's constant)	

$$U_{front} = \frac{A_{front}(h_{air} + h_{sky})}{A_{front} + h_{air} + h_{sky}} \qquad (17)$$

$$U_{back} = \frac{A_{back}(h_{air} + h_{wat})}{A_{back} + h_{air} + h_{wat}} \qquad (18)$$

The sky temperature is computed from Eq. (11).

5. Validation

Together with the heat balance model, the nominal operating condition temperature (NOCT) provided by the module manufacturer was used to validate the CFD model. NOCT is the temperature of the cells (T_{NOCT}) at a plane-of-array (POA) solar irradiance of 800 W/m^2 (G_{NOCT}), an ambient air temperature of 20 °C ($T_{a,NOCT}$), a wind speed of 1 m/s, and for modules that are mounted in an open rack.

PV panels deployed on the pond in Marlenique are glass-polymer CS6U-330 (330 W) modules manufactured by Canadian Solar. In the datasheet, T_{NOCT} of the module is specified to 45 ± 2 °C (Canadian Solar, 2022). A CFD computation of a free-standing module tilted by an angle of 15°, subject to NOCT conditions and without a float, gives an average cell temperature of 47.5 °C. This is just outside the temperature interval specified by the module manufacturer. A contour plot of the resulting temperatures, which also reveals the simplified geometry, is shown in Fig. 6a. The symmetry plane of the model is shown, as is the main wind direction which is identified by the white arrow. Based on the heat balance model described in Section 4, T_{NOCT} was computed to 46.5 °C. Results, summarized in Table 5, show that the CFD model reproduces well the value for T_{NOCT} specified by Canadian Solar (2022). Satisfactory agreement was also obtained between the heat balance model and the CFD model.

Fig. 6b displays an extended CFD computations which also includes the float. Otherwise, the calculation was identical to the one used to produce the results in Fig. 6a. It reveals that the presence of the float increases the average cell temperature from 47.5 °C to 50.4 °C. Fig. 6b also displays that the float promotes a significant non-uniform temperature field in the wafer layer, with temperatures above the float body warmer than at the module short ends which are better ventilated. If 85% of the solar irradiation is converted to heat in the cells, the U-value computed from Eq. (20) becomes 25.6 W/m^{2}K for the case without a float and 22.4 W/m^{2}K including the float. The difference in U-value, 3.2 W/m^{2}K, is useful information when values for an array of modules mounted to floats are evaluated and discussed in Section 7.

6. Parameter study

As Eq. (1) shows, it is well-known that low operating cell temperature is linked to enhanced efficiency of PV modules. For glass-polymer modules mounted to Ciel et Terre floats and exposed to various weather conditions, the focus of this parameter study was to examine the importance of solar irradiation, air temperature, water temperature and wind speed on the resulting cell temperatures and U-values. The model included a row of 18 modules, as depicted in Fig. 2. Wind comes in from the left and hits the first panel, in the figure labelled "1", at an angle of 15°, which is the tilt angle of the modules. Convective cooling of the first module in the row is largely unaffected by downstream modules and walkways. The air flow past the other modules in the row is disturbed by upstream modules and/or walkways, which thus affects how well these are cooled.
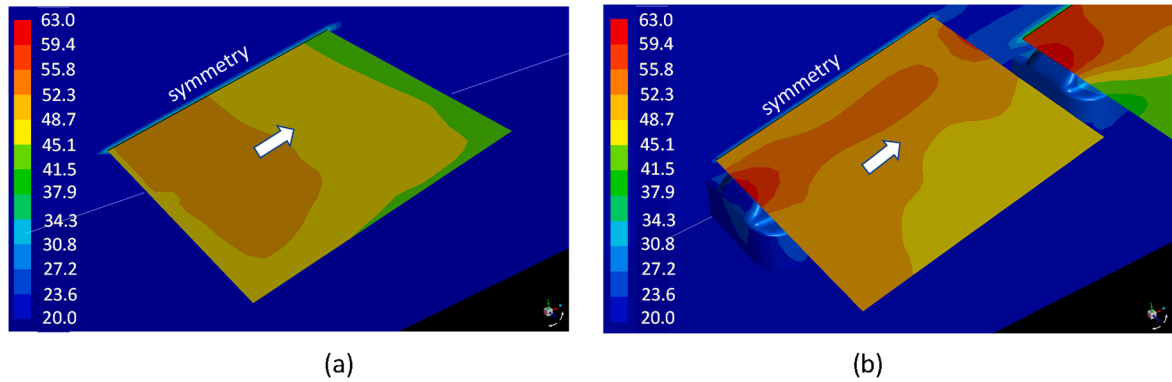
Fig. 6. Contour plots of temperatures in a module tilted by an angle of 15°. (a) Well-ventilated module without float. (b) Module mounted to a Ciel et Terre float.

Table 5
T_{NOCT} from manufacturer and computations.

Datasheet (Canadian Solar)	45 ± 2 °C
CFD (ANSYS Fluent)	47.5 °C
Heat balance model	46.5 °C

Two heat transfer mechanisms were disregarded in the study. Firstly, evaporation of water and water sprays have potential to enhance the heat loss of FPV modules (Nižetić et al., 2016). Secondly, humidity has the potential to affect the atmosphere around the PV module and the module temperature, thereby affecting the power performance of the PV module (Choi et al., 2021). FPV plants based on Ciel et Terre's floater technology, HDPE float structures with PV modules installed at a low tilt angle, are typically located in regions with high water temperature. Categorized as a FPV technology with large water footprint, the parameter study considered PV-modules working under these regional and environmental assumptions.

Four cases that are summarized in Table 6 were defined. Case 1, which was the base case, assumed a solar irradiance of 800 W/m², an air temperature of 25 °C, and a water temperature that is 5 °C lower than the ambient air. Energy converted to heat in the cells was assumed to be 85% of the solar irradiation. The influence of solar irradiance on the cell temperatures and U-values was examined in Case 2. With unchanged air and water temperatures, the solar irradiance was increased to 1000 W/m². Case 3 considered the influence of the ambient air temperature on the cell temperatures and U-values. Combined with the same level of solar irradiance as in Case 2, the air and water temperature were both increased by 5 °C in Case 3. In Case 4, the temperatures in air and water were both set to 30 °C to cancel out the influence of this temperature difference. For all four cases, computations were carried out accounting for wind speeds ranging from 1 m/s to 5 m/s. Cell temperatures and U-values of the individual 18 modules along the row were then compared.

6.1. Case 1 (G_T = 800 W/m², T_{air} = 25 °C, T_{air} - T_{wat} = 5 °C)

For Case 1 and a wind speed of 3 m/s, contour plots of the resulting cell temperatures are shown in Fig. 7. The resulting temperature field is strongly non-uniform, with the part above the float significantly warmer than at the sides. This is a likely situation as the air flow in the gap between the float and PV module is restricted by the float. Much better

Table 6
Parameters in the study.

Parameter	Case 1	Case 2	Case 3	Case 4
Solar irradiance [W/m²]	800	1000	1000	1000
Air temperature [°C]	25	25	30	30
Water temperature [°C]	20	20	25	30

cooling is achieved on the sides, which also have a small contribution of radiative heat transfer to the water body.

While average cell temperatures computed for Case 1 are shown in Fig. 8a, U-values are included in Fig. 8b. Based on Eq. (11), the U-values were derived from the equation.

$$U = \frac{(\tau\alpha - \eta_c) \bullet G_T}{(T_{cell} - T_{air})} \tag{24}$$

where all values on the right-hand side, except the cell temperature, were input to the CFD model. In both parts of Fig. 8, the horizontal axis identifies the module position in the row. The front row module is labelled #1. As seen from Fig. 2, every third module is followed by a walkway. Fig. 8a clearly shows that cooling is significantly improved by increased wind speed. In general, the first 3 or 4 modules in the row are slightly better cooled that those downstream. A cyclic pattern of the curves is observed for the computed cell temperatures of other modules in the row. If modules separated by walkways are grouped and examined, the cell temperature of the module in the middle was computed to be lower than for the two others. How the U-values are influenced is revealed in Fig. 8b. The curves exhibit local minimums and maximums that are amplified with increasing wind speed. This behavior is caused by the convective heat transfer, see h_{air} in Eq. (21), which becomes more important at windy conditions. For the lowest wind speed, 1 m/s, the variation of the derived U-values is small along the row of modules, as it varies between 21.0 W/m²K and 23.7 W/m²K. The corresponding variation for the largest wind speed, 5 m/s, is from 39.2 W/m²K to 51.2 W/m²K. These results demonstrate the significant influence the wind speed has on the module U-value.

6.2. U-values and cell temperatures

A summarization of computed cell temperatures versus the wind speed for all four cases defined in Table 6 is shown in Fig. 9a. It includes two sets of curves: one for the front row module (continuous lines) and another that represent the average cell temperature of all modules in the row (dotted lines). Corresponding U-values are shown in Fig. 9b. It shows that the U-value based on the average cell temperature of the module row is lower than the U-value of the front row module, which has a more advantageous air flow that is unaffected by other modules and walkways. It also shows that the U-value increases linearly with the wind speed. FPV field test data reveal a similar relationship between the U-value and the wind speed (Dörenkämper et al., 2021).

6.3. Case 2: Influence of solar irradiance

With solar irradiance increased from 800 W/m² (Case 1) to 1000 W/m² (Case 2), Fig. 9a and Fig. 9b reveal the influence on the cell temperatures and the U-values. For wind speeds in the range from 1 m/s to 5 m/s, the average cell temperature representing all modules in the row
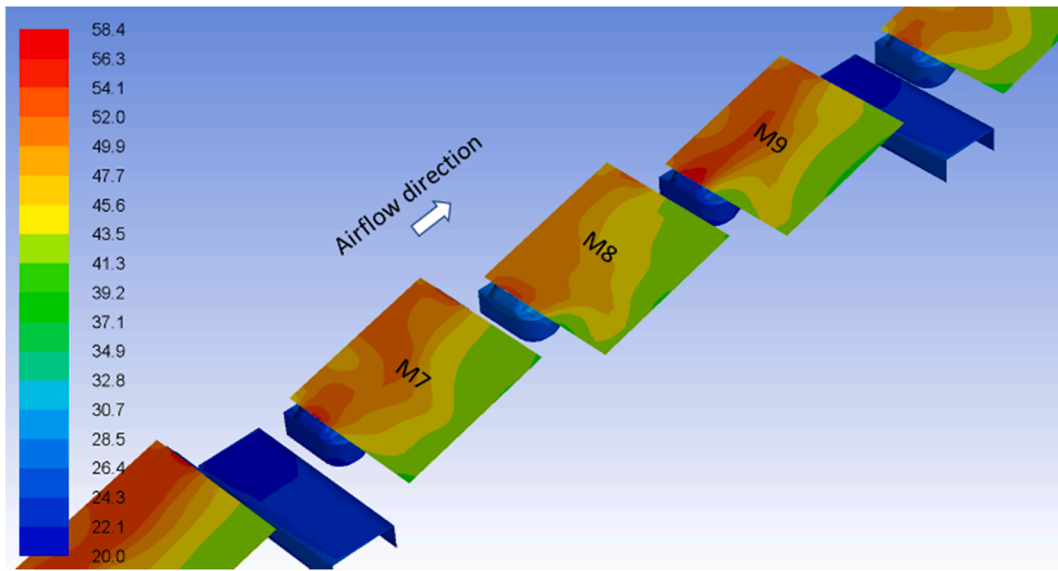
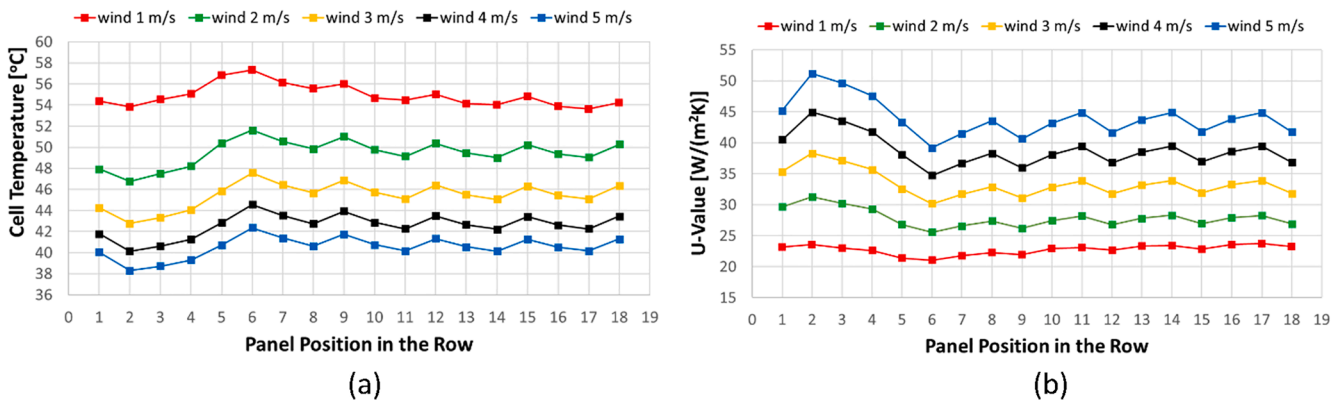**Fig. 7.** Cell temperatures obtained for Case 1 with wind speed equal to 3 m/s.

Fig. 8. Results obtained for Case 1: $G_T = 800$ W/m^2, $T_{air} = 25$ °C, and $T_{wat} = 20$ °C. (a) Computed cell temperature. (b) Derived U-values.
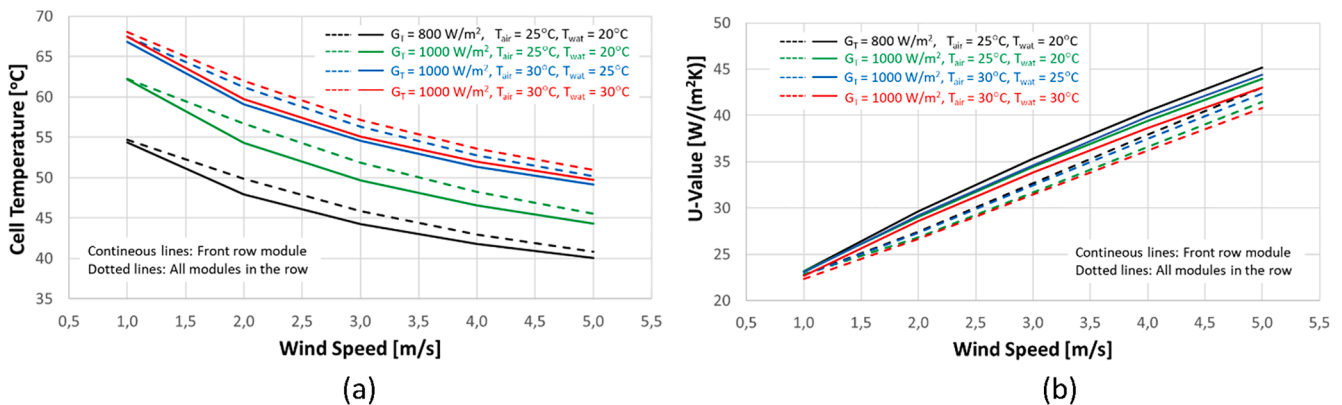

Fig. 9. Results obtained for Case 1 to 4. Part (a): cell temperatures obtained for the front row module and the average cell temperature of all modules in the row. Part (b): U-values obtained for the front row module and the average U-values of all modules in the row.

increased by 4.7 to 7.4 °C. The largest increase was obtained for the lowest wind speed. For ground-based PV (GPV), Faiman's model (Faiman, 2008) is commonly used to compute the operational cell temperature. It divides the U-value into two terms, one that is constant and a second that scales with the wind velocity,

$$U = U_0 + U_1 \cdot v_{air} \tag{25}$$

The CFD computations showed a weak dependency of the U-value on the solar irradiation. When it increased from 800 W/m^2 to 1000 W/m^2, the U-value dropped between 0.1 and 1.6 W/m^{2}K. The reason can be explained by the simpler heat balance model in Section 4. While the cell

temperature in Eq. (13) is directly dependent on the solar irradiance, the U-value has a weaker dependency in Eqs. (22) and (23), which include module temperatures that account for radiative heat transfer to the sky and the water. As a conclusion, although the influence on the cell temperature is significant, the level of solar irradiation has small influence on the U-value for the modules mounted to Ciel et Terre floats.

6.4. Case 3: Influence of air temperature

Case 2 and 3 were used to examine the influence of the air temperature on the cell temperature and module U-value. Both cases assumed high level of the solar irradiation (1000 W/m^2) and a water temperature 5 °C colder than the air temperature. The air temperature was increased from 25 °C in Case 2 to 30 °C in Case 3. Based on these assumptions, Fig. 9a shows that the average cell temperature increased by 4.7 to 5.3 °C. The effect on the U-values is small and comparable to that obtained between Case 1 and 2. For the type of module and float technology examined in the study, the increase in cell temperature is about on same level as the increase in air temperature. For the U-value, the increased air temperature has small influence.

6.5. Case 4: Influence of water temperature

The final comparison in the parameter study was to consider the influence of the water temperature. Case 3 and 4 assume both a solar irradiation of 1000 W/m^2 and an air temperature of 30 °C. In Case 3 the water was 5 °C colder than air, while in Case 4 this difference was canceled out. In the CFD model, water provides mainly radiative cooling of the modules. Potentially, air below the modules is convectively cooled by the water, which enables air to pick up more heat from the modules. When the air–water temperature difference drops from 5.0 °C to 0.0 °C, Fig. 9a shows that the average cell temperature of the modules in the row increases by 0.4 to 0.7 °C, which means that the water temperature does not significantly influence the cell temperature. Despite the small change in cell temperature, the difference in U-value is about 1.5 W/m^2 at a wind speed of 5 m/s.

6.6. Comparison to a reference ground-based PV module

For FPV technologies with large water footprint, our study concludes that the water temperature itself has small influence on the cell temperature and the module U-value. However, the ambient air above the water body is typically windier and colder than above the ground. For an air-cooled FPV module lifted some distance above the water surface, Liu et al. (2017) used FEM modelling to compare the cell temperature against a reference, horizontally aligned ground-mounted PV module. With the ambient air temperature above the water body set 5 °C colder than the corresponding temperature above the ground, 25 °C vs. 30 °C, the computed cell temperature difference was 3.5 °C in favor of the FPV module. The computation was based on $G_T = 1000$ W/m^2 and a wind speed of 1 m/s. No CFD computation was performed, and the convective heat transfer coefficient on the module front side was computed from.

$$h_{air} = 8.55 + 2.56 \cdot v_{air} \qquad (26)$$

The convective heat transfer coefficient on the module back side was set to half the value at the front. For the same input of G_T and wind speed, our CFD model based on Case 2 and 4 predicted 5.9 °C in favor of the FPV module. However, Liu et al. (2017) did not account for a temperature difference between the water body and the ambient air above the water body, as in Case 2. If the water is 5.0 °C colder than the air temperature above, comparison of Case 3 and 4 reveals that the radiative heat transfer contribution constitutes a difference of 0.6 °C in cell temperature. Excluding radiative heat transfer between the water and the module backside, our model therefore predicts 5.3 °C in favor of the FPV module. Considered the difference in methodology, this temperature difference compares well with that computed by Liu et al. (2017).

7. Comparison to field measurements

Recently, Dörenkämper et al. (2021) published a comparison between U-values derived from FPV field data obtained from two different climate zones: the Tenghe reservoir in Singapore (tropical climate) and the Netherlands (temperate maritime climate). Based on the extent of water surface coverage beneath the modules and the capability of air to cool the back of the modules, FPV technologies were categorized according to the water footprint. For technologies based on large water footprint, the wind-dependent U-values derived from the two FPV test sites were.

$$U = 34.8 + 0.8 v_{air} (Singapore) \qquad (27)$$

$$U = 25.2 + 3.7 v_{air} (the Netherlands) \qquad (28)$$

The basis for Eq. (27) is a FPV system with direct exposure to water, but the float structure and module's proximity to water reduces the ability of air to cool the back of the module. Eq. (28) is based on a technology with modules that have no direct water exposure and that are fixed to concrete floats. The latter technology facilitates for better ventilation beneath the modules, which is reflected in the wind-dependent term of the equation.

Together with curves that represent Eqs. (27) and (28), a corresponding curve derived from our CFD computations is displayed in Fig. 10. The computations, which correspond to Case 1 in Section 6, were based on an irradiation of 800 W/m^2, an air temperature of 25 °C and a water temperature of 20 °C. The curves account for wind speeds ranging from 1 m/s to 5 m/s. As for the measurements, the computations provided a curve that increases linearly with the wind speed. However, the dependency on the wind speed is stronger, and compared to the experimental-based curves it predicts lower U-values for wind velocities less than 3.5 m/s and larger U-values for wind speed above 3.7 m/s. The curve based on CFD obeys the linear equation.

$$U = 17.7 + 5.5 \cdot v_{air} \qquad (29)$$

U-values derived from CFD were generally closer to the experimental values obtained in the Netherlands. Perfect match between the curves was neither expected nor achieved, but the agreement to U-values derived from field data is considered acceptable and the model well suited for parameter studies.

Results obtained by CFD computations for a single PV module with and without a float were compared in Section 5. The U-value without a float was computed to be 3.2 W/m^{2}K larger. The heat balance model in Section 4 computed almost identical T_{NOCT} as the CFD model with the float omitted, therefore also the same U-value. The curve labelled "Our Study (heat balance model)" in Fig. 10 represents U-values computed by the heat balance model, but for solar irradiation of 800 W/m^2, air
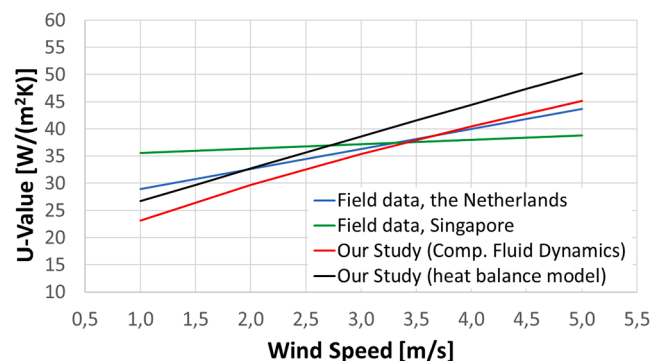

Fig. 10. U-values versus wind speed for FPV technologies with large water footprint. U-values derived from field data in the Netherlands and Singapore (Dörenkämper et al., 2021) are compared to similar results obtained from CFD and from the heat balance model.

temperature of 25 °C, and water temperature of 20 °C. In general, it exhibits larger U-values than the CFD calculation, which is reasonable as the presence of the float decreases the cooling and therefore also the U-value. The difference in U-value increases from 3.6 W/m^{2}K at 1 m/s wind speed to 5.0 W/m^{2}K at 5 m/s. The fact that the CFD computations provide lower U-values than in simplified heat balance calculations, is supported by the model validation in Section 5. It adds confidence that the CFD results obtained for an array of modules mounted to Ciel et Terre floats are reasonable.

8. Conclusions

It is well-known that low operating temperature promotes high cell efficiency. As air above a water body is typically colder and windier than on land, it is often claimed that floating solar technologies has better efficiency than ground-based systems. Few have quantified this effect, which is further complicated by the diversity of float structures. For a specific float technology with large water footprint, low tilt angle of the PV modules and for a location with relatively warm water, the aim of this study was to use CFD to quantify the cooling effect of modules deployed on a water body. Today, the FPV market is dominated by systems consisting of float structures such as the solution developed by Ciel et Terre. This technology was therefore chosen to quantify cell temperatures and U-values.

In the datasheet provided by the module manufacturer, NOCT is specified to 45 ± 2 °C. For NOCT conditions and without the float, the CFD model computed an average cell temperature of 47.5 °C. By inclusion of the float, the CFD model predicted the average cell temperature to increase from 47.5 °C to 50.4 °C. The presence of the float itself, which represents a loss in U-value of about 3.2 W/m^{2}K, causes a highly non-uniform temperature field in the wafer layer.

The parameter study confirm that solar irradiation and ambient air temperature does not have significant influence on the U-value. The U-value was found to vary linearly from 23.2 W/m^{2}K (1 m/s) to 45.2 W/m^{2}K (5 m/s) and depend on the wind velocity according to Eq. (29). The cell temperature rises significantly by decreasing wind velocity, and by increasing solar irradiation and air temperature. We also find that the water temperature does not significantly affect the U-value. Radiative heat transfer between the back of the module and water was estimated to reduce the cell temperature typically less than 1 °C.

For FPV technologies with large water footprint, our study concludes that the water temperature itself has small influence on the cell temperature and the module U-value. However, the ambient air above the water body is typically windier and colder than above the ground. A comparison between a 15° tilted PV module above a water body (ambient air temperature of 25 °C) and a corresponding reference ground-based PV-module (ambient air temperature of 30 °C), gave a cell temperature difference of 5.3 °C in favor of FPV. This compares well to similar values reported in the literature.

Published U-values derived from FPV field data in Singapore and the Netherlands show a similar linear dependency of the wind as predicted by our CFD model. However, the dependence is stronger for the specific technology we have studied. Because the technologies are not identical but still represent systems with large water footprint, U-values from our study were considered to compare well to U-values derived from field data.

Declaration of Competing Interest

The authors declare that they have no known competing financial interests or personal relationships that could have appeared to influence the work reported in this paper.

Acknowledgements

References

Appelbaum, J., Maor, T., 2020. Dependence of PV module temperature on incident time-dependent solar spectrum. App. Sci. 10 (3), 914. https://doi.org/10.3390/app10030914.

Bellini, E., 2022. World's largest floating PV plant goes online in China. PV Magazine. https://www.pv-magazine.com/2022/01/03/worlds-largest-floating-pv-plant-goes-online-in-china/. (Accessed 3 February 2022).

Cazzaniga, R., Rosa-Clot, M., 2021. The booming of floating PV. Sol. Energy 219, 3–10. https://doi.org/10.1016/j.solener.2020.09.057.

Canadian Solar, 2022. Maxpower CS6U-330|335|340|345M. Datasheet downloaded 3rd February 2022 from the website of Canadian Solar (www.canadiansolar.com).

Choi, J.H., Hyun, J.H., Lee, W., Bhang, B.G., Min, Y.K., Ahn, H.K., 2021. Power performance of high density photovoltaic module using energy balance model under high humidity environment. Sol. Energy 219, 50–57. https://doi.org/10.1016/j.solener.2020.10.022.

Dörenkämper, M., Wahed, A., Kumar, A., De Jong, M., Kroon, J., Reindl, T., 2021. The cooling effect of floating PV in two different climate zones: A comparison of field test data from the Netherlands and Singapore. Sol. Energy 214, 239–247. https://doi.org/10.1016/j.solener.2020.11.029.

Dubey, S., Sarvaiya, J.N., Seshadri, B., 2013. Temperature dependent photovoltaic (PV) efficiency and its effect on PV production in the world - a review. Energy Procedia 33, 311–321. https://doi.org/10.1016/j.egypro.2013.05.072.

Evangelisti, L., Guattari, C., Asdrubali, F., 2019. On the sky temperature models and their influence on buildings energy performance: A critical review. Energy Build. 183, 607–625. https://doi.org/10.1016/j.enbuild.2018.11.037.

Faiman, D., 2008. Assessing the outdoor operating temperature of photovoltaic modules. Prog. Photovoltaics Res. Appl. 16 (4), 307–315.

Filipović, P., Dović, D., Ranilović, B., Horvat, I., 2019. Numerical and experimental approach for evaluation of thermal performances of a polymer solar collector. Renew. Sustain. Energy Rev. 112, 127–139.

Fouad, M.M., Shihata, L.A., Morgan, E.S.I., 2017. An integrated review of factors influencing the performance of photovoltaic panels. Renew. Sustain. Energy Rev. 80, 1499–1511. https://doi.org/10.1016/j.egypro.2019.01.139.

Gonzalez Sanchez, R., Kougias, I., Moner-Girona, M., Fahl, F., Jäger-Waldau, A., 2021. Assessment of FPV potential in existing hydro reservoirs in Africa. Renew. Sustain. Energy Rev. 169, 687–699. https://doi.org/10.1016/j.renene.2021.01.041.

Hammami, M., Torretti, S., Grimaccia, F., Grandi, G., 2017. Thermal and performance analysis of a photovoltaic module with an integrated energy storage system. App. Sci. 11, 1107. https://doi.org/10.3390/app7111107.

Haugwitz, F., 2020. Floating solar PV gains global momentum. PV Magazine. https://www.pv-magazine.com/2020/09/22/floating-solar-pv-gains-global-momentum/. (Accessed 3 February 2022).

IEA PVPS, 2021. Trends in photovoltaic applications 2021. International Energy Agency Photovoltaic Power Systems Programme. Report IEA-PVPS T1-41:2021. ISBN 978-3-907281-28-4.

Kim, K., Song, T.-H., 2010. Discrete ordinates interpolation method incorporated into a flow and energy solver for solution of combined heat transfer problems. J. Quant. Spectrosc. Radiat. Transfer 111 (14), 2070–2083. https://doi.org/10.1016/j.jqsrt.2010.05.003.

Lee, N., Grunwald, U., Rosenlieb, E., Mirletz, H., Aznar, A., Spencer, R., Cox, S., 2020. Hybrid FPV-hydropower systems: Benefits and global assessment of technical potential. Renew. Sustain. Energy Rev. 162, 1415–1427. https://doi.org/10.1016/j.renene.2020.08.080.

Lindholm, D., Kjeldstad, T., Selj, J., Marstein, E.S., Fjær, H.G., 2021. Heat loss coefficients computed for floating PV modules. Prog. Photovoltaics Res. Appl. 29 (12), 1262–1273. https://doi.org/10.1002/pip.3451.

Liu, L., Wang, Q., Lin, H., Li, H., Sun, Q., Wennersten, R., 2017. Power generation efficiency and prospects of floating photovoltaic systems. Energy Procedia 105, 1136–1142. https://doi.org/10.1016/j.egypro.2017.03.483.

Liu, H., Krishna, V., Lun Leung, J., Reindl, T., Zhao, L.u., 2018. Field experience and performance analysis of floating PV technologies in the tropics. Prog. Photovoltaics Res. Appl. 26 (12), 957–967. https://doi.org/10.1002/pip.3039.

Mohammed, H., Gupta, R., Sastry, O., Magare, D., 2019. Assessment of different correlations to estimate distinct technology PV module operating temperature for Indian site. Energy Sci. Eng. 7, 1032–1041. https://doi.org/10.1002/ese3.332.

Moreno, J., Casado, C., Marugán, J., 2019. Improved discrete ordinate method for accurate simulation radiation transport using solar and LED light sources. Chem. Eng. Sci. 205, 151–164. https://doi.org/10.1016/j.ces.2019.04.034.

Nižetić, S., Čoko, D., Yadav, A., Grubišić-Čabo, F., 2016. Water spray cooling technique applied on a photovoltaic panel: The performance response. Energy Convers. Manage. 108, 287–296. https://doi.org/10.1016/j.enconman.2015.10.079.

Ogbomo, O.O., Amalu, E.H., Ekere, N.N., Olagbegi, P.O., 2018. Effect of operating temperature on degradation of solder joints in crystalline silicon photovoltaic modules for improved reliability in hot climates. Sol. Energy 170, 682–693. https://doi.org/10.1016/j.solener.2018.06.007.

Oliveira-Pinto, S., Stokkermans, J., 2020. Assessment of the potential of different floating solar technologies – Overview and analysis of different case studies. Energy Convers. Manage. 211, 112747. https://doi.org/10.1016/j.enconman.2020.112747.

Reindl, T., 2018. World's largest floating solar testbed - overview & findings. ACEF Deep Dive Workshop on Floating Solar (June 8, 2018).

Skoplaki, E., Palyvos, J.A., 2009. On the temperature dependence of photovoltaic module electrical performance: a review of efficiency/power correlations. Sol. Energy 83 (5), 614–624. https://doi.org/10.1016/j.solener.2008.10.008.

Solheim, H.J., Fjær, H.G., Sørheim, E.A., Foss, S.E., 2013. Measurement and simulation of hot spots in solar cells. Energy Procedia 38, 183–189. https://doi.org/10.1016/j.egypro.2013.07.266.

Swinbank, W.C., 1963. Long-wave radiation from clear skies. Quarterly Journal of Royal Meteorological Society 89 (381), 339–348.

Watmuff, J.H., Charters, W.W.S., Proctor, D., 1977. Solar and wind induced external coefficients solar collectors. Revue Internationale Heliotechnique 2, 56.

Where Sun Meets Water, 2019. Floating Solar Handbook for Practitioners, World Bank Group and SERIS, Singapore.